Nuclear Materials and Energy 28 (2021) 101048

Contents lists available at ScienceDirect

Nuclear Materials and Energy

journal homepage: www.elsevier.com/locate/nme

Modeling and experimental validation of a W_f/W-fabrication by chemical vapor deposition and infiltration

L. Raumann [a,b,*], J.W. Coenen [a,c], J. Riesch [d], Y. Mao [a], D. Schwalenberg [a], T. Wegener [a], H. Gietl [e], T. Höschen [d], Ch. Linsmeier [a], O. Guillon [a,b,f]

[a] Forschungszentrum Jülich GmbH, Institute for Energy and Climate Research, 52428 Jülich, Germany[1]
[b] Institute of Mineral Engineering, Rheinisch-Westfälische Technische Hochschule Aachen, 52062 Aachen, Germany
[c] Department of Engineering Physics, University of Wisconsin - Madison, Madison, WI 53706, USA
[d] Max-Planck-Institute for Plasma Physics, 85748 Garching b. München, Germany
[e] Oak Ridge National Laboratory, Oak Ridge, TN 37830, USA
[f] JARA-Energy, Jülich Aachen Research Alliance, Germany

ARTICLE INFO

Keywords:
Chemical vapor deposition/infiltration
Tungsten fiber reinforced tungsten
Comsol multiphysics
Macroscopic reactor model
Microscopic pore formation model
Scripted metallographic image analysis

ABSTRACT

Tungsten (W) has a unique combination of excellent thermal properties, low sputter yield, low hydrogen retention, and acceptable activation. Therefore, W is presently the main candidate for the first wall material in future fusion devices. However, its intrinsic brittleness and its further embrittlement during operation bears the risk of a sudden and catastrophic component failure. As a countermeasure, tungsten fiber-reinforced tungsten (W_f/W) with extrinsic toughening is being developed. A possible synthesis route is chemical vapor deposition (CVD) using heated W fabrics as substrate. The challenge is that the growing CVD-W can isolate domains from precursor access leading to strength-reducing pores. To deepen the process understanding and to optimize the CVD parameters, models were developed with COMSOL Multiphysics and validated experimentally. W deposition rate equations as function of the temperature and the partial pressures of the precursors H_2 and WF_6 were experimentally validated in previous work. In the present article, these equations are applied to obtain partial pressures within the CVD reactor. The results are taken as input for transient simulations in the microscale, in which W coatings, growing onto multiple adjacent W fibers, were simulated via mesh deformation and remeshing. The surface-to-surface contact of the W coatings and the corresponding potential pore formation were simulated by implementing sophisticated deposition rate stop conditions. Within the measuring uncertainties of $\simeq \pm 1\%$, the models are validated successfully by experimental comparison regarding the deposition rate, pore structure, and relative densities ranging from 0.6 to 0.9.

1. Introduction

To realize commercial fusion power plants the development of high-performance materials with adequate lifetimes is essential. One of the ultimate reactor-design challenges is to deal with the enormous heat and particle fluxes, plasma erosion, neutron irradiation, and transmutation [1–4]. Tungsten (W) is currently the main candidate material, as it well meets most of these requirements [5,6]. As all pure metals, tungsten has a high thermal conductivity. Further, it has the highest melting point of all metals (3695 K) and a high plasma erosion resistance. The reason for these properties is the combination of a high atomic number ($Z = 74$) and a high atomic binding energy (approx. 11.8 eV [7]), which is e.g. approx. 4.6 times the binding energy of lead (Pb, $Z = 82$) [8]. However, polycrystalline tungsten has the drawback of a high ductile-to-brittle transition temperature (DBTT), which ranges from 300–1200 K, depending on the fabrication process and treatment [9,10]. Furthermore, it is suspected to increase by several hundreds Kelvin due to neutron irradiation within a year of fusion operation [11,12].

Studies have shown that thermal stresses induced by transient events during plasma instabilities can lead to the failure of complete plasma-facing components consisting of W sheet material [13]. This is particularly problematic for smaller reactor designs, which have even higher material requirements. New materials are being developed to overcome this issue [14]. One of these new materials is a tungsten fiber-reinforced tungsten (W_f/W) composite, in analogy to fiber-reinforced ceramics [12,14–19]. Due to the increased toughness and damage

* Corresponding author at: Forschungszentrum Jülich GmbH, Institute for Energy and Climate Research, 52428 Jülich, Germany.
E-mail address: l.raumann@fz-juelich.de (L. Raumann).
[1] Partner in the Trilateral Euregio Cluster.

https://doi.org/10.1016/j.nme.2021.101048
Received 19 April 2021; Received in revised form 9 July 2021; Accepted 26 July 2021
Available online 31 July 2021

Nomenclature

i, j	Placeholders for species (here WF_6, H_2, HF or W)
A	Area [m^2]
$D_{eff,i}$	Effective ordinary diffusion coefficient [$m^2\ s^{-1}$]
D_{ij}	Binary ordinary diffusion coefficient [$m^2\ s^{-1}$]
$D_{Kn,i}$	Knudsen diffusion coefficient [$m^2\ s^{-1}$]
$D_{T,i}$	Thermal diffusion coefficient [$kg\ m^{-1}\ s^{-1}$]
$d_{decel.start}$	Surface-to-surface distance below which the surfaces are decelerated [m]
d_{final}	Final surface-to-surface distance [m]
E_A	Activation energy [$J\ mol^{-1}$]
k_0, k_1, k_2	Constants for deposition rate equations [$m\ s^{-1}\ Pa^{-(n_{H_2}+n_{WF_6})}$]
k_B	Boltzmann constant [$1.381 \times 10^{-23}\ J\ K^{-1}$]
L_{char}	Characteristic length between nearest walls [m]
N	Number of gas species [–]
n_i	Reaction order [–]
P_{tot}	Total pressure [Pa]
p_i	Partial pressure [Pa]
R	Gas constant [$8.314\ J\ mol^{-1}\ K^{-1}$]
R_W	Deposition rate of W [$m\ s^{-1}$]
$R_{WF_6 dep.}$	R_W, dependent on p_{WF_6} [$m\ s^{-1}$]
$R_{WF_6 indep.}$	R_W, independent on p_{WF_6} [$m\ s^{-1}$]
R^2	Coefficient of determination [–]
T	Temperature [K]
Δt	Deposition duration [s]
$\dot{V}_i$	Volume flow rate [sccm]
x_i	Mole fraction [–]
ρ_{rel}	Relative density [–]

Abbreviations

CVD	Chemical vapor deposition
DBBT	ductile-to-brittle transition temperature
FEM	Finite element method
W	Tungsten
W_f/W	Tungsten fiber-reinforced tungsten

resistance below the DBTT of pure W, W_f/W is expected to provide longer lifetimes, especially after neutron irradiation [20].

As first step to produce W_f/W, potassium doped drawn W fibers are coated by a thin layer (currently Y_2O_3 is coated by physical vapor deposition), which must have a weaker fracture energy than the W fibers. The reason is that it later has to function as a fiber–matrix-interface, which enables crack energy dissipating mechanisms within the W_f/W composite [21]. These mechanism provide pseudoductility despite of a brittle matrix [22,23]. As next step, the coated fibers are embedded in the W matrix. Besides powder metallurgy utilizing short fibers [24–26], chemical vapor deposition (CVD) on long fibers or fabrics [27,28] is a possible synthesis route. For this work, CVD was used with tungsten hexafluoride (WF_6) and hydrogen (H_2) as gaseous precursors. They react on surfaces heated above 550 K to solid W with high purity [29] and gaseous hydrofluoric acid, as described by Eq. (1).

$$WF_6(g) + 3H_2(g) \rightarrow W(s) + 6HF(g) \quad (1)$$

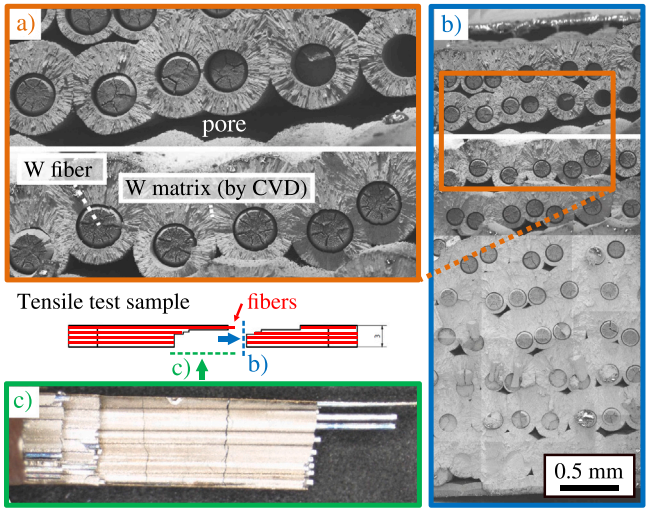

Fig. 1. Fracture surface of a W_f/W tensile test specimen that has delaminated due to too large pores. More details can be found in [30].

One of the major process challenges is that pores can remain, if the solid W matrix growing from adjacent fibers connects and seals off gaseous domains from the precursor supply. These pores in the matrix between the fibers weaken the mechanical properties of the composite, as they lead to a stress concentration which could lead to a premature matrix crack initiation and delamination of coated layers, as it happened in the tensile test specimen shown in Fig. 1.

The porosity can be reduced by increasing the fiber-to-fiber distances, however this reduces also the fiber fraction and hence the fiber reinforcing effect. Therefore, the current work was motivated by the question whether the porosity in W_f/W can also be reduced by just optimizing the CVD process parameters (temperature, gas flow rates and pressure) without decreasing the fiber fraction. To answer this question, CVD models were developed utilizing the commercial Finite Element Method (FEM) software COMSOL Multiphysics [31] (from now on referred to as Comsol).

The first development step focused on the influence of the CVD process parameters on the W deposition rate, presented in [32]. The present article focuses on applying the W deposition rate equations to model and experimentally validate the infiltration of multiple adjacent fibers within a W fabric. The fabric, which is also the CVD substrate, can be seen in Fig. 2.

The working procedure for the present article is summarized in Fig. 3. The W_f/W produced by W-CVD on a W fabric was evaluated microscopically regarding fiber positions and relative densities. For the models a multi-scaled approach was chosen. A macro-scaled stationary model, named “Reactor Model”, took as input the mean fiber positions and the experimental CVD process parameters. As output the Reactor Model returned spatially resolved partial pressures above the fibers, which were taken as input for a separate and transient microscaled model, named “Single Pore Model”. Additional inputs were the detailed fiber positions from the experimentally evaluated W_f/W cross-section. As output, the Single Pore Model returned the relative density (ρ_{rel}) around each pore (45 in total), which were compared to the experimental results to validate the models.

2. Experimental procedure

2.1. W_f/W production

The W fabric (Fig. 2) was produced by weaving W fibers with a shuttle loom followed by a roll to flatten the fabric via plastic deformation of the weft fibers [27,33].

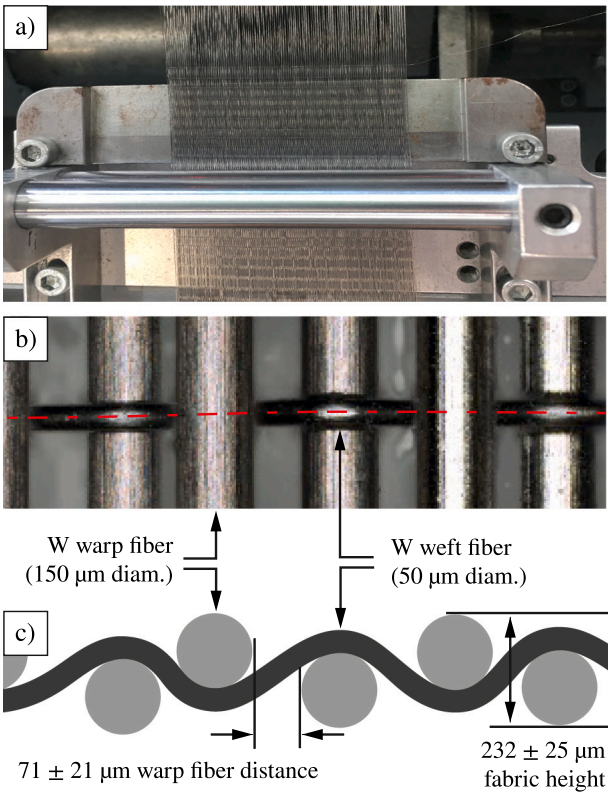

Fig. 2. (a) W fibers (top) and fabric (bottom) within a paused shuttle loom (weaving machine), (b) Close-up of a W weft fiber and W warp fibers, (c) sketch of a cross-sectional slice showing the fabric dimensions, whereby the weft fiber distance (missing third dimension) was approx. 3 mm.

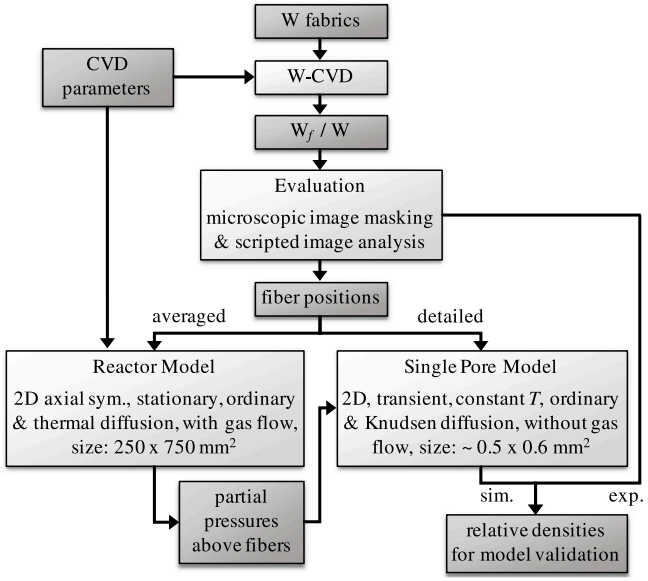

Fig. 3. Flow chart illustrating the procedure of the presented work; with the methods and models in light gray, and the inputs and outputs in dark gray.

5×5 cm^2 fabric pieces were clamped into frames for straightening and coated via physical vapor deposition with a 1–2 µm thick Y_2O_3 interface. Next, the fabric was placed onto a heating table located inside of a bell-shaped vessel (radius 0.5 m, height 0.75 m), to which the gas inlets, the vacuum pumps, and the exhaust gas handling was connected. The base pressure of the chamber was < 0.1 kPa. During heating up an

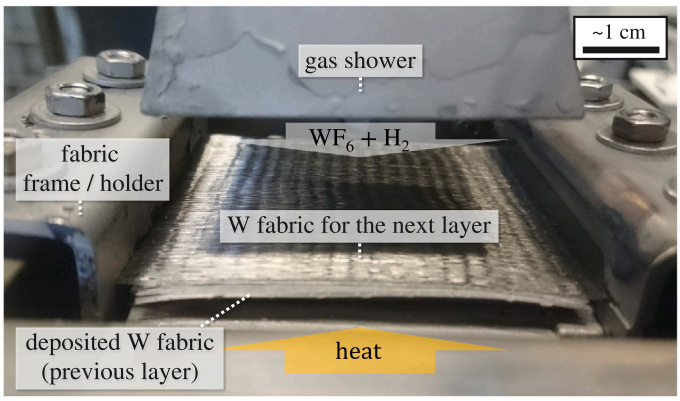

Fig. 4. Picture of a W_f/W production step: a fabric was mounted on previously coated fabric layers grown onto the heating table inside of the CVD chamber.

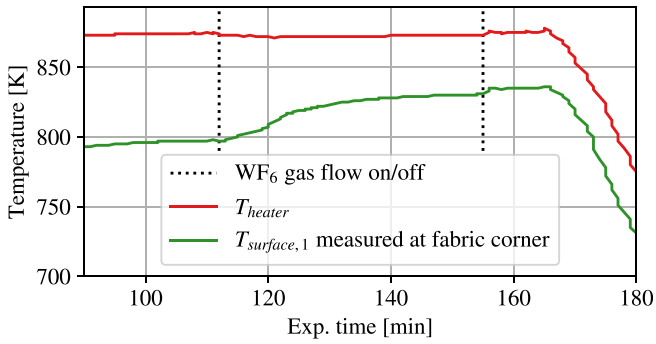

Fig. 5. Different temperatures vs. experimental time.

Table 1
CVD process parameters used for the first layerwise W_f/W production. For the symbols please see the Nomenclature.

T_{heater}	873	K
$T_{surface,1}$	797–831	K
P_{tot}	9.5	kPa
$\dot{V}^{inlet}_{H_2}$	1500	sccm
$\dot{V}^{inlet}_{WF_6}$	400	sccm
Δt	45	min

Ar and H_2 flow was sent vertically to the center of the fabric. After thermal equilibrium was reached, the Ar flow was replaced by WF_6 to start the W deposition. A picture of a mounted fabric is shown in Fig. 4.

A thermocouple in the inner of the heating table was used to hold T_{heater} at 873 K. Another thermocouple (for $T_{surface,1}$) was placed onto an outer edge of the fabric. During the deposition $T_{surface,1}$ started at 797 K and increased asymptotically to 831 K as shown in Fig. 5. The surface temperatures are lower than the heating temperature due to gas flow cooling and heat radiation losses. The reason for the surface temperature increase is that the thermal conductive contact between the fabric and the thermocouple is improved over time while the CVD-W grows around them. The temperatures and the other applied CVD process parameters are listed in Table 1.

The here investigated W_f/W composite was produced layerwise, as developed in [18], in the frame-work of an experimental fiber–fiber-distance parameter study [34]. The sample with the closest mean warp fiber distance (Fig. 2c) was chosen to be simulated, to obtain a strong precursor depletion inside of pores for a clearer model validation.

2.2. W_f/W evaluation

The W_f/W sample was cut and polished perpendicular to the warp fiber axes. It was investigated with an optical microscope (Zeiss) in the

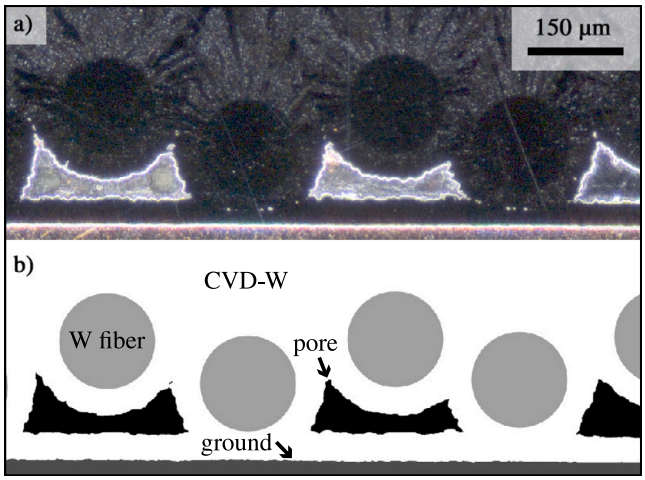

Fig. 6. Example for the image masking procedure with (a) input: dark-field optical microscopic image, (b) output: masked areas for the CVD-W (white), the W fibers (light gray), the pore areas (black), and the ground/heating plate (dark gray).

dark field mode at maximum microscope brightness. This was necessary to avoid that the W_f/W porosity appears too large due to light scattering at the W edges rounded off by polishing. The correctness of this method was validated using a Scanning Electron Microscope (Zeiss DSM 982 Gemini).

The ground (heating plate) and the pores were masked semi-automatically using a combination of the magic wand tool, selection enlargement, and area filling in Adobe Photoshop. Sections of the unmasked and masked microscope image are shown in Fig. 6(a) and (b), respectively. As measuring uncertainty the pore area selections were enlarged or reduced by ±2 pixels (= ±1 µm), which changed e.g. a mid-sized pore area having approx. 70.000 by approx. ±3.000 pixels. The warp fibers (91 in total), were masked by transparent 150 µm circles. As measuring uncertainty of the fiber positions ±1 µm shifts in x- and y-direction were taken.

Taking the masked images as input, the warp fiber coordinates and relative densities (ρ_{rel}) were obtained via scripted image analysis around each pore between three adjacent warp fibers. The fiber center coordinates were obtained using the Python library "Skimage" [35]. Based on the coordinates, an area, named control area, was defined around each pore, in which the relative density (ρ_{rel}) was calculated and compared to the simulation. Such a control area is visualized in green in Fig. 7 and calculated by Eq. (2a). The pore areas were obtained by summing up the black pixels. Finally, ρ_{rel} was calculated via Eq. (2b). The respective Python script can be downloaded from [36].

$$A_{control} = x_2\frac{y_1 + y_2}{2} + (x_3 - x_2)\frac{y_2 + y_3}{2} \tag{2a}$$

$$\rho_{rel} = 1 - \frac{A_{pore}}{A_{control}} \tag{2b}$$

with

$A_{control}$:	Control area	[µm^2]
x, y :	Local fiber center coordinates	[µm]
1, 2, 3:	Left, middle, and right fiber	
ρ_{rel} :	Relative density	[–]
A_{pore} :	Pore area	[m^2]

3. Model descriptions

3.1. Reactor model

The Comsol model of the CVD reactor was developed to obtain an estimate for the species partial pressures above the fabric needed as input for the microscaled Single Pore Model (as depicted in the bottom left of Fig. 3). The Reactor model was simulated stationary. The Comsol model file for the Reactor Model as well as for the later described Single Pore Model can be downloaded from [36].

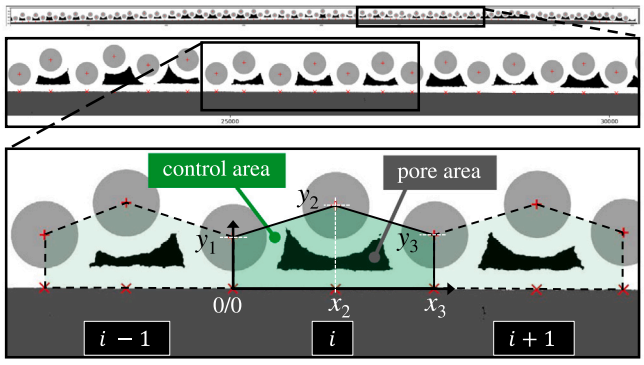

Fig. 7. Scheme for the evaluation of the fiber coordinates and the pore area of a pore i. (For interpretation of the references to color in this figure legend, the reader is referred to the web version of this article.)

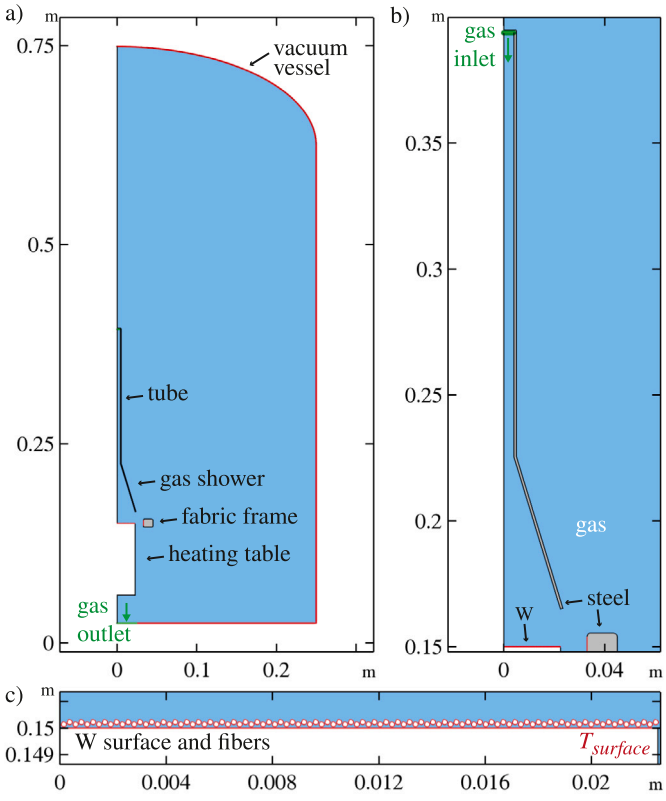

Fig. 8. (a) Reactor Model geometries with a close-up of the gas shower in (b), and the heated W fibers in (c).

3.1.1. Geometry and boundary conditions

The model geometry is shown in Fig. 8. As in the experiment, the gas enters at approx. 523 K with the same flow rates through a steel pipe connected to a gas shower, which is aligned over the W-fibers and the heating table. The simulation was done in 2D for simplification and faster calculations. Despite of the square shape of the fabric, an axial symmetry was chosen as it results with the 2D-constraint in the most realistic gas flow behavior: as in the experiment the gas enters through a tube and spreads radially in all directions when hitting the plate.

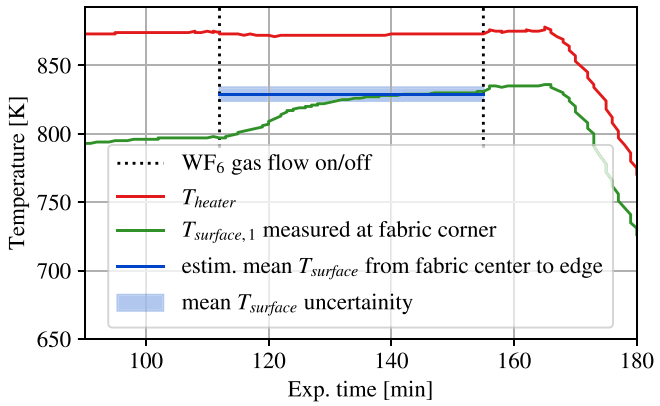

Fig. 9. Different temperatures ($T_{surface}$) vs. experimental time with an estimation of mean $T_{surface}$, averaged over time and from the fabric center to the edge. The estimation is based on the experimentally coated thickness and on deposition rate modeling. (For interpretation of the references to color in this figure legend, the reader is referred to the web version of this article.)

The fibers were modeled via two circles that were cloned by two arrays. The circle centers equaled the mean values from the experimental image analysis. As the fibers are coated with CVD-W, their outer radii and thus their total reaction area grow until their surfaces contact after a period of time Δt_c. To account for the resulting increased mean precursor consumption compared to the initial radius, the stationary modeled radius was increased to a value that a transiently modeled radius would have reached after $\Delta t_c/2$. This is approximately the initial radius (here 75 µm) plus a quarter of the distance between two adjacent fiber surfaces (here 21.3 µm).

Since in previous work the experimental temperature was well known in a different setup designed for obtaining the W deposition rate equation [32], in this work the rate equation was used to deduce the experimental surface temperature $T_{surface}$ from the experimental deposition rate. In detail, the mean value and uncertainty of $T_{surface}$ was obtained iteratively to be 829 ± 5 K (Fig. 9, blue line), by matching the simulated W coating thicknesses on top of the upper fibers towards the experimental coating thicknesses at the same locations (from center to the outer edge, perpendicular to the warp fiber axes).

3.1.2. Chemistry and rate equations

The chemical reactions at the heated surfaces were described by fast solving simplified rate Eqs. (3), (3a) and (3b) as experimentally validated in [32]. The species mass fluxes towards (WF_6, H_2) and from (HF) the reactive surfaces are calculated via the stoichiometry, resulting from Eq. (1), in conjunction with the reaction rate (Eq. (3)). The heat of reaction is calculated via the thermodynamic properties of the species as listed in [32].

$$R_{W,sim} = \min(R_{WF_6 indep.}, R_{WF_6 dep.}) \tag{3}$$

with $R_{WF_6 dep.}$ from Eq. (3a) and $R_{WF_6 indep.}$ from Eq. (3b).

$$R_{WF_6 dep.} = \left(\frac{1}{k_1\, p_{WF_6}} + \frac{1}{k_2 \exp\left(\frac{-E_A}{RT}\right) [p_{H_2}]^{1/2} [p_{WF_6}]^{1/6}} \right)^{-1} \tag{3a}$$

with E_A = 64 kJ/mol, k_1 = (32.63 ± 2.88) ×10^{-9} m s^{-1} Pa^{-1} and k_2 = (45.79 ± 1.28) ×10^{-7} m s^{-1} $Pa^{-2/3}$ [37].

$$R_{WF_6 indep.} = k_0 \exp\left(\frac{-E_A}{RT}\right) [p_{H_2}]^{1/2} [p_{WF_6}]^{0} \tag{3b}$$

with E_A = (73.7 ± 0.9) kJ/mol and k_0 = (38.22 ± 4.85) × 10^{-6} m s^{-1} $Pa^{-1/2}$ [32]. The equations are for H_2:WF_6 ratios ≥ 3.

Table 2
Polynomials a_0, a_1 and a_2 to calculate D_{ij} according to Eq. (4) [32].

ij	a_0 [Pa m^2 s^{-1}]	a_1 [Pa K^{-1} m^2 s^{-1}]	a_2 [Pa K^{-2} m^2 s^{-1}]
H_2 WF_6	−2.518	1.521×10^{-2}	1.459×10^{-5}
HF WF_6	-6.384×10^{-1}	2.922×10^{-3}	5.583×10^{-6}
H_2 HF	−4.832	2.885×10^{-2}	3.498×10^{-5}

3.1.3. Fluid dynamics and heat transfer

The gas mixture is considered as continuum. For the mono-species H_2, WF_6, and HF, the heat capacity was fitted to tabulated data from [38]. The gas density, dynamic viscosity, and thermal conductivity are calculated from the Lennard-Jones parameters (ϵ/K_B, σ, and μ_D) as in [39]. The values used are tabulated in [32]. The spatially resolved gas mixture properties are calculated by Comsol [31] based on the mono-species values and the local mass fractions. Similar equations can be found in [40].

The Reynolds number Re reaches values of 1200–1300 only in a small model-coaxial cylindric domain (10 mm height, 1 mm radius) within the gas shower, where chemical reactions do not take place yet. Potential eddies ($Re_{crit} \approx 1200$) would dissipate quickly before reaching the reaction surface and would thus not affect the CVD modeling results. Therefore, it was decided to model the gas flow with Comsol's laminar flow interface [31]. For simulating thermal conduction, convection, and radiation, Comsol's inbuilt functions were used without modifications [31].

3.1.4. Diffusion

Diffusion can be sectioned into ordinary diffusion driven by concentration gradients, into thermal diffusion driven by temperature gradients, and into Knudsen diffusion taking into account gas-solid interactions at gap widths in the range of the free mean path of the gas molecules.

Since the macroscaled Reactor Model is stationary, the distances between the fibers remain large enough to neglect Knudsen diffusion. Ordinary diffusion was calculated via the Stefan–Maxwell formulation described in [41]. For this the Comsol interface "transport of concentrated species" needs as input binary diffusion coefficients (D_{ij}) for all involved species pairs. D_{ij} were calculated by Eq. (4) as derived in [32] for the gas mixture with WF_6, H_2, and HF (N = 3).

$$D_{ij} = \sum_{k=0}^{2} \frac{a_k \cdot T^k}{P_{tot}} \tag{4}$$

with a_0, a_1, a_2 listed in Table 2.

Thermal diffusion describes the effect that in a fluid, which contains heavy as well as light molecules, heavy molecules are repelled from hot domains and thus light molecules are concentrated in these domains [42]. Heavy molecules (such as WF_6) have a positive thermal diffusion coefficient (D_T) and light molecules (such as H_2) a negative D_T [43]. Due to thermal gradients towards the heated reaction surfaces, thermal diffusion becomes relevant for the Reactor Model. For a given gas mixture, $D_{T,i}$ depends only on T and the mole fractions (x_i). However, the calculation includes the division of the determinants of a ($2N \times 2N$)- and a ($2N \times 2N + 1$)-matrix, whereby each element of the matrices has to be calculated by formulas involving the gas species properties [39]. To save a lot of computational effort a Python script was written [36], which prepares the values for $D_{T,i}$ as a lookup table that can be imported and interpolated in Comsol. In Fig. 10 D_{T,WF_6}, D_{T,H_2}, and $D_{T,HF}$ are plotted for different T and for an x_i slice from 25% WF_6 and 75% H_2 to 100% HF.

3.2. Single Pore Model

The Single Pore Model is capable of predicting the microscaled pore size and shape after CVD on the first fabric layer. This was achieved by a transient mesh deformation, which moved the solid surfaces into the gas domain with the same velocity as the W deposition rate (R_W).

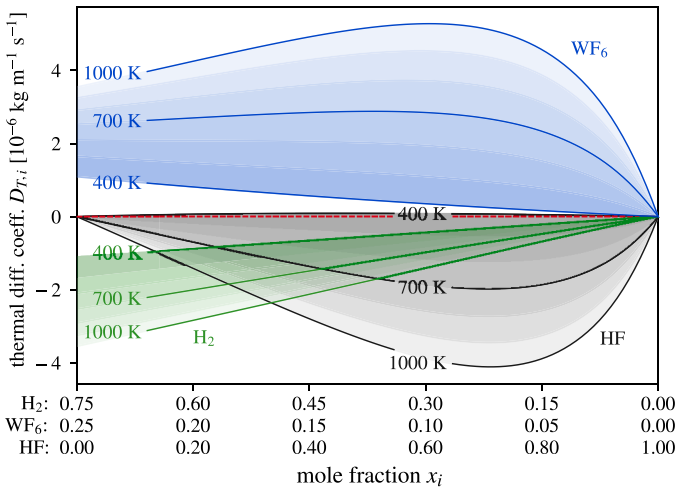

Fig. 10. Thermal diffusion coefficients of H_2, WF_6 and HF as function of gas composition and T.

3.2.1. Chemistry and rate equations

The same rate equations as in the Reactor Model were used. However, to achieve faster convergence and a higher model robustness, practically irrelevant low deposition rates, due to the WF_6 consumption inside of the pores, were not considered. This was achieved by multiplying $R_{W,sim}$ (Eq. (3)) with a smoothed step function being 1 for WF_6 gas concentrations $\geq 1 \times 10^{-5}$ mol/m^3 and zero for $\leq 1 \times 10^{-6}$ mol/m^3. For comparison, inlet concentrations were ≈ 0.25 mol/m^3.

3.2.2. Geometry and boundary conditions

In Fig. 11 the geometry and boundary conditions of the Single Pore Model are shown. The model was chosen to be 2D without axial symmetry, which matches better to the experiment in this microscale. The temperature in the entire model was set constant to the experimentally measured T_{surf}. The partial pressure at the top boundary (p_i^{top}) was taken from the Reactor Model results at the corresponding height and heating plate radius (r). Species transport within the gas domain was modeled via diffusion only. At the gaseous geometric side boundaries the species fluxes were set to zero. The growth of the W coating and thus deformation of the reactive surfaces is taken into account via Comsol's deforming mesh interface, which was configured as shown in (Fig. 11b). The cyan boundaries equal the dark blue boundaries until the pore is sealed. After sealing, the flux and motion is stopped at the dark blue boundary. Since the geometry changes drastically over time, Comsol's standard settings for the chosen free triangular mesh and for the solver had to be changed as described in the Appendix in Appendix A.1.

3.2.3. Pore sealing workarounds

In the experiment, the W coating grows on adjacent fibers until it unites to a single connected solid domain creating potentially a sealed gas domain. However, in the Comsol version used (v. 5.4) two separate solid domains cannot be merged transiently and new domains cannot be created during the simulation. All domains need to be defined from the start on. Further, the simulation fails when the surface meshes start to overlap, which happens by using a constant time step size. For a variable time step size, the simulation will take infinitely long as the time steps and wall distance become infinitely small as the surfaces approach each other.

To solve this problem, the reaction surfaces moving with a velocity equal to the W deposition rate (R_W) were decelerated at a gap size $d_{decel.start}$ and stopped at d_{final} by multiplying R_W with a step function (f_{step}) plotted in Fig. 12. Larger values for d_{final} and $d_{decel.start}$ improve the simulation speed and robustness, but can lead to a too fast diffusion. $d_{decel.start}$ = 4 μm and d_{final} =2 μm showed a good compromise regarding speed and robustness with negligible influence on the results.

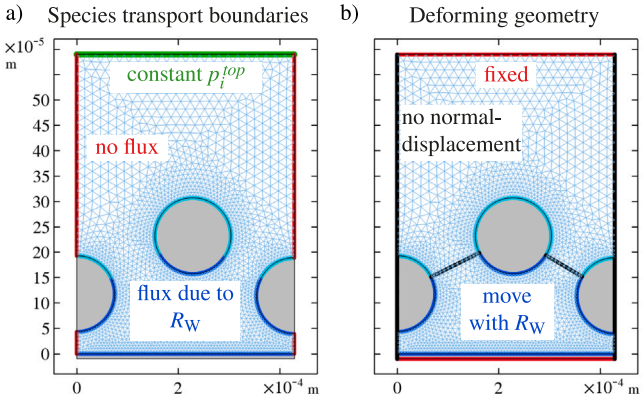

Fig. 11. Single Pore Model boundaries for (a) species transport, (b) deforming geometry. Following figures with the same geometry as in this figure have the same axes. (For interpretation of the references to color in this figure legend, the reader is referred to the web version of this article.)

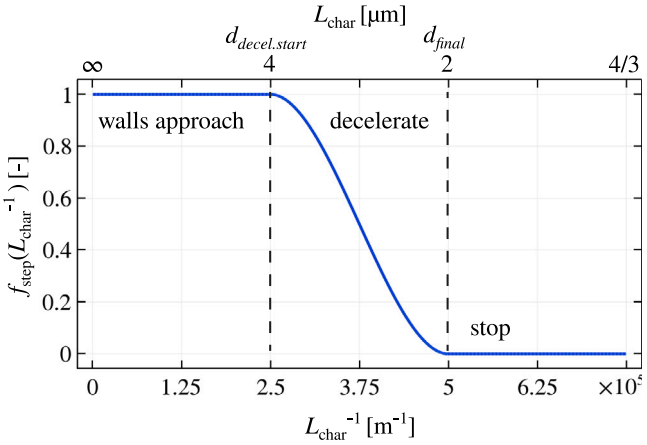

Fig. 12. Smoothed step function $f_{step}([L_{char}]^{-1})$, which is multiplied with R_W to decelerate R_W for $L_{char} \leq d_{decel.start}$ and to set R_W to zero for $L_{char} \leq d_{final}$.

To track the gap size between all nearest surfaces in form of a transient and spatial variable, needed as input for f_{step}, a characteristic length (L_{char}) was defined by Eq. (5).

$$L_{char} = \min\left(d_{w,s,f_{1,3}} + d_{w,f_2},\ d_{w,s,f_{1,3}} + d_{w,g},\ d_{w,f_2} + d_{w,g}\right) \quad (5)$$

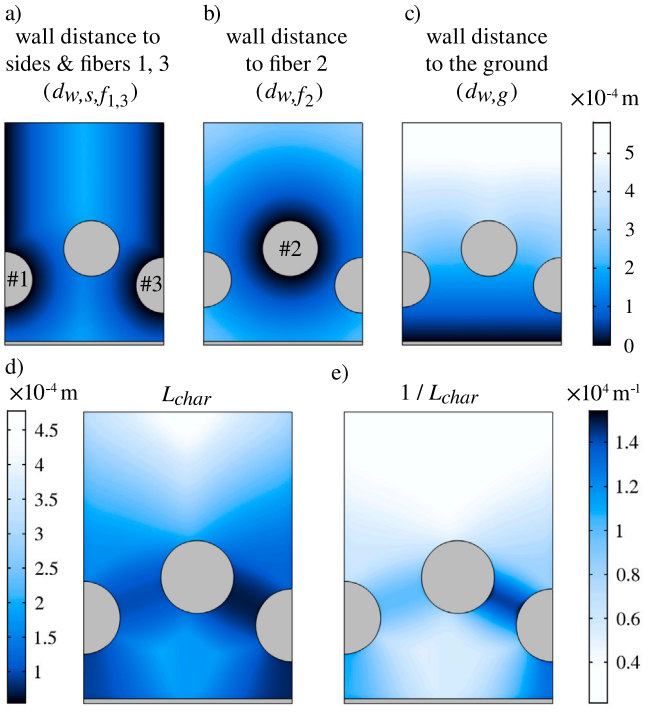

Fig. 13. 2D color maps for (a) the wall distances $d_{w,s,f_{1,3}}$, d_{w,f_2}, and $d_{w,g}$, (b) characteristic length between nearest walls L_{char} (Eq. (5)), and (c) $[L_{char}]^{-1}$, which can be seen as a field variable tracking the wall to wall distance very sensitively with respect to smaller gap sizes.

with $d_{w,s,f_{1,3}}$, d_{w,f_2}, and $d_{w,g}$ being the distances to separated wall parts as shown in Fig. 13a, b, and c, respectively.

Eq. (5) returns the minimum of all wall distance pair-sums, which equals the nearest wall-to-wall distance and thus the needed variable L_{char} shown in Fig. 13d. To understand Eq. (5) better: If one looks at an arbitrary imaginary point in the blue color map in Fig. 13d, for example between the middle fiber (#2) and the right fiber (#3), L_{char} equals the distance towards the nearest surface of fiber #2 plus the distance towards the nearest surface of fiber #3. Moving the imaginary point in parallel to the connection line of the fiber centers (#2-#3) does not change L_{char}. Moving further out of the gap increases L_{char}, as it should be.

By taking the reciprocal of L_{char} (Fig. 13e) as argument for f_{step} (Fig. 12) the simulation solves faster and becomes more robust. The reason is that $[L_{char}]^{-1}$ changes the more, the closer the walls get; therefore, $[L_{char}]^{-1}$ is more sensitive within the distance range being of interest for decelerating and stopping R_W.

The gap-workaround described above solves the first problem (mesh collision or infinitely long simulation), however, it causes a new problem. The gas species can diffuse through the artificial gap into the pore, even if it is only 2 µm broad or less. This phenomenon keeps the deposition reaction and thus pore filling going, which would have stopped already in reality.

Therefore, a stop condition needs to be applied on R_W within the pore after the pore got sealed. The challenge is to find the correct sealing time step. Taking the time step when the gap size reaches d_{final} does not work as this event is delayed by the technically needed deceleration. Therefore, instead of tracking the fiber radii along the direct connection between the fiber centers (l), they are tracked at an angle ω (Fig. 14). ω (Eq. (6)) is the angle at which the sum of the simulated fiber radii ($r_1(t)+r_2(t)$) reaches l, when the pore would have been sealed at a single virtual contact point without being affected by the artificial deceleration. Based on this, the transient stop condition,

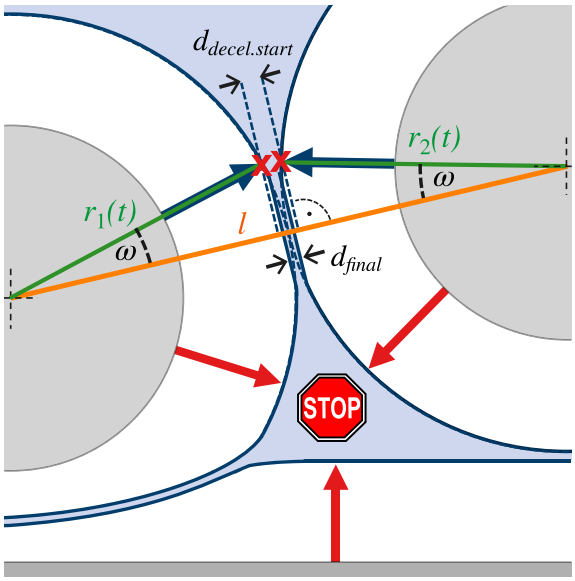

Fig. 14. Illustration of the workaround for the surface-to-surface contact problem in Comsol. $d_{decel.start}$ is the distance between the transiently simulated CVD surfaces, at which the surfaces start to decelerate from R_W towards zero (compare to Fig. 12). l is the distance between the fiber centers. $r(t)$ is the fiber radius plus the transient coating thickness at an angle ω towards l so that the point at the surface (×) is as close as possible to the pseudocontact point, while still being unaffected by the deceleration of R_W.

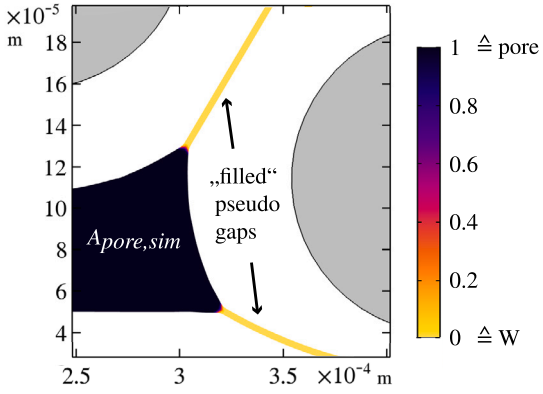

Fig. 15. Color map for $f_{step}\left((L_{char}-d_{final}/2)^{-1}\right)$ plotted within A'_{pore}. For the pore area integration black is counted as one (pore) and yellow as zero (solid).

shown in Eq. (7), was implemented to stop R_W within the pore at a realistic time step.

$$\omega = \arccos\left(\frac{\frac{l}{2}-\frac{d_{decel.start}}{2}}{\frac{l}{2}}\right) = \arccos\left(1-\frac{d_{decel.start}}{l}\right) \tag{6}$$

$$\text{when} \quad r_1(t)+r_2(t) \geq l: \quad R_W \text{ in pore} = 0 \tag{7}$$

3.2.4. Diffusion

Since thermal gradients can be neglected in the Single Pore Model, there is also no thermal diffusion. However, Knudsen diffusion becomes relevant as the surfaces of adjacent fibers approaches to wall distances in the order of magnitude of the free mean path of the gas molecules. Therefore, the ordinary diffusion is slowed down by collisions between the gas molecules and the wall, which was taken into account by implementing the Knudsen diffusion coefficient ($D_{Kn,i}$, Eq. (8)) [44,45].

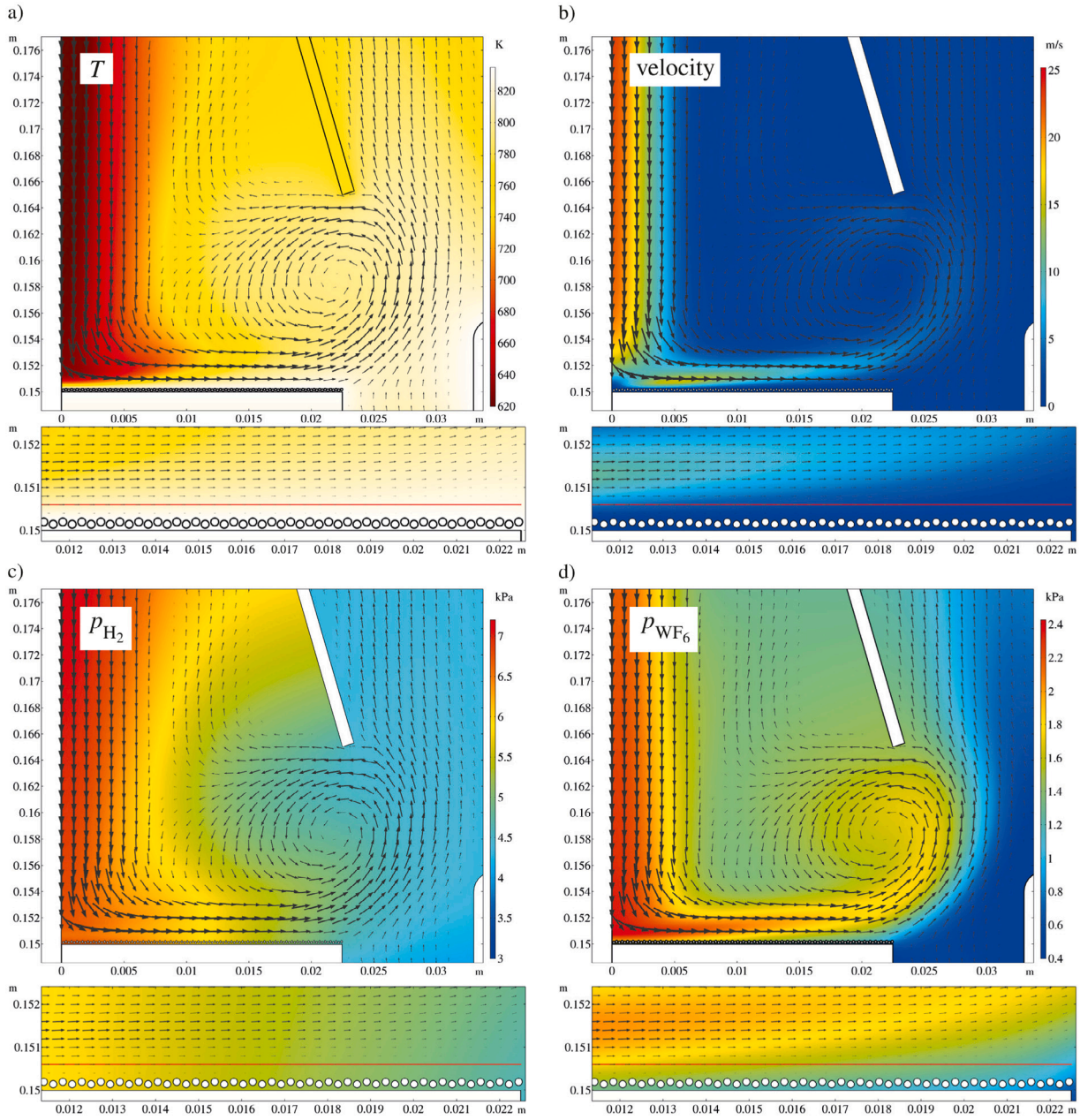

Fig. 16. Color maps for (a) temperature (T), (b) gas flow speed, (c) H_2 partial pressure (p_{H_2}), and (d) WF_6 partial pressure (p_{WF_6}) vs. the Reactor Model coordinates (y: height, x: radius). The black vectors represent the total gas flow direction and speed. The sections show the area below the gas shower and a further zoom towards the W fibers. The red line marks from where the partial pressures were taken as input for the upper boundary of the Single Pore Model. (For interpretation of the references to color in this figure legend, the reader is referred to the web version of this article.)

$$D_{Kn,i} = \frac{d}{3} \cdot \left(\frac{8RT}{\pi M_i} \right)^{\frac{1}{2}} \tag{8}$$

with d being the gap width of an infiltrated trench. In the Single Pore Model, the transient and spatial variable L_{char} (Eq. (5)) was taken for d.

The ordinary diffusion description via the Maxwell–Stephan formulation is not compatible with Knudsen diffusion. The reason is that for the Knudsen diffusion one coefficient per species i is obtained; however, the Maxwell–Stephan formulation consists always of a set of differential equations taking into account all involved spatial dimensions at once. Therefore, in order to implement Knudsen diffusion, the ordinary diffusion was modeled following the Wilke approximation [46], which returns via Eq. (9) also a single mixture-averaged effective (ordinary) diffusion coefficient ($D_{eff,i}$) per species i.

$$D_{eff,i} = (1 - x_i) \left(\sum_{i=1, j \neq i}^{N} \frac{x_j}{D_{ij}} \right)^{-1} \tag{9}$$

To implement Knudsen diffusion, the mixture-averaged ordinary diffusion coefficient ($D_{eff,i}$) was replaced by $D'_{eff,Kn,i}$ (Eq. (10)), which changes the more from $D_{eff,i}$ towards the Knudsen diffusion coefficient ($D_{Kn,i}$, Eq. (8)) the smaller the gap size becomes.

$$D'_{eff,Kn,i} = \left(\frac{1}{D_{eff,i}} + \frac{1}{D_{Kn,i}} \right)^{-1} \tag{10}$$

3.2.5. Calculation of the simulated relative density

The simulated relative densities ($\rho_{rel,sim}$) around the pores are calculated in the same way as for the experimental results (Eq. (2)), except

Table 3
Averaged results based on the W_f/W evaluation of 45 pores within the first fabric layer. The coordinates are as illustrated in Fig. 7.

Fiber center coordinates [µm]				exp. rel. density ($\rho_{rel,exp}$) [%]		
	mean	un-cert.	std. dev.	mean	un-cert.	std. dev.
x_1	0.0	±1.0	±0.0	77.3	±1.1	±7.3
x_2	222.7	±1.0	±21.6			
x_3	441.0	±1.0	±22.0			
y_1	142.7	±1.0	±25.3			
y_2	225.8	±1.0	±24.3	Fiber volume fraction [%]		
y_3	143.4	±1.0	±25.1	22.5		±2.5

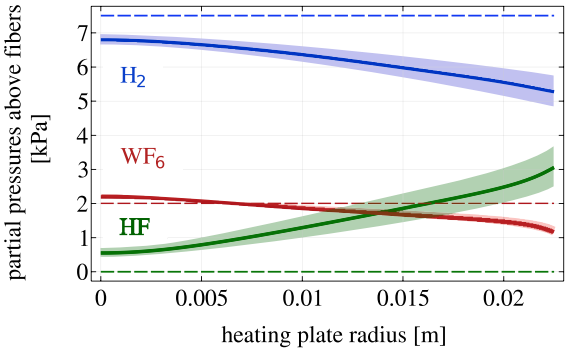

Fig. 17. Partial pressures p_i above the fibers for H_2, WF_6, and HF versus the heating plate radius. (——): simulation result with transparent areas showing the influence of the 10 K uncertainty in T_{surf}, (- - -): estimation based solely on the inlet gas flow ratio and the total pressure.

that the simulated pore area ($A_{pore,sim}$) is acquired differently. Instead of counting pixels a Comsol-internal area integration of the earlier presented step function (Fig. 12) is used. Before calculating the relative density from the simulated pore structure, the artificial gaps, which were needed to avoid mesh collision during the simulation, are filled with solid W (yellow stripes in Fig. 15). This was achieved by modifying the argument of f_{step} from L_{char} to $(L_{char} - d_{final}/2)^{-1}$ as shown in Eq. (11).

$$A_{pore,sim} = \oint_0^{A'_{pore,sim}} f_{step}\left((L_{char} - d_{final}/2)^{-1}\right) dA \tag{11}$$

with

$A'_{pore,sim}$	: pore area including the artificial gap [m^2]
$A_{pore,sim}$	: (corrected) pore area without the gap [m^2]
f_{step}	: step function (Fig. 12) with $(L_{char} - d_{final}/2)^{-1}$ as argument [–]

4. Results and discussion

4.1. Experimental

The mean experimental results from the scripted image analysis of the W_f/W polish (Fig. 7) are shown in Table 3. The detailed values for each pore can be found in [47].

The large standard deviations of the fiber coordinates and the mean relative density ($\rho_{rel,exp}$) are advantageous for the Single Pore Model validation since they allow for the variations necessary for a solid model validation. Each pore can be seen as individual small experiment with its own fiber positions and ρ_{rel}.

4.2. Reactor model

Fig. 16 shows 2D maps of the quasi stationary equilibrium in the Reactor Model for the quantities T, the gas flow speed, p_{H_2}, and p_{WF_6}.

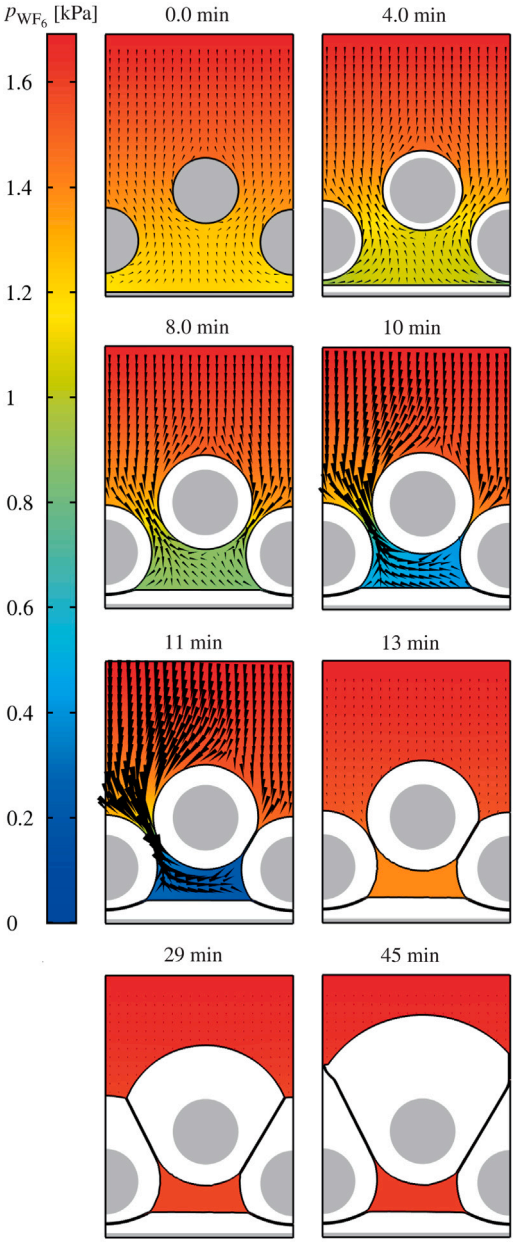

Fig. 18. Frame series for the Single Pore Model (pore #0). Gray domains: substrate (fibers and ground), white domains: growing CVD-W, colored domains: gas, showing p_{WF_6} with black arrows for the total diffusive flux of WF_6. (For interpretation of the references to color in this figure legend, the reader is referred to the web version of this article.)

The gas streams out from the gas shower, hits the fabric, is heated up and redirected in radial direction. The precursors WF_6 and H_2 are consumed along and between the hot substrate (ground and fibers), thus p_{H_2} and p_{WF_6} decrease.

From the Reactor Model result several simplifications were deduced for the model setup and boundary conditions of the Single Pore Model. Fig. 16a shows that T is constant around the fibers and within the pores. Fig. 16b shows that the gas flow provides the precursors near the upper fiber surface, whereby the gas flow between the fibers is close to zero (Fig. 16b) and the major species transport into the pores takes place by diffusion. Therefore, in the Single Pore Model the gas flow can be neglected and the species transport can be modeled based on diffusion only with the top boundary having constant p_i values.

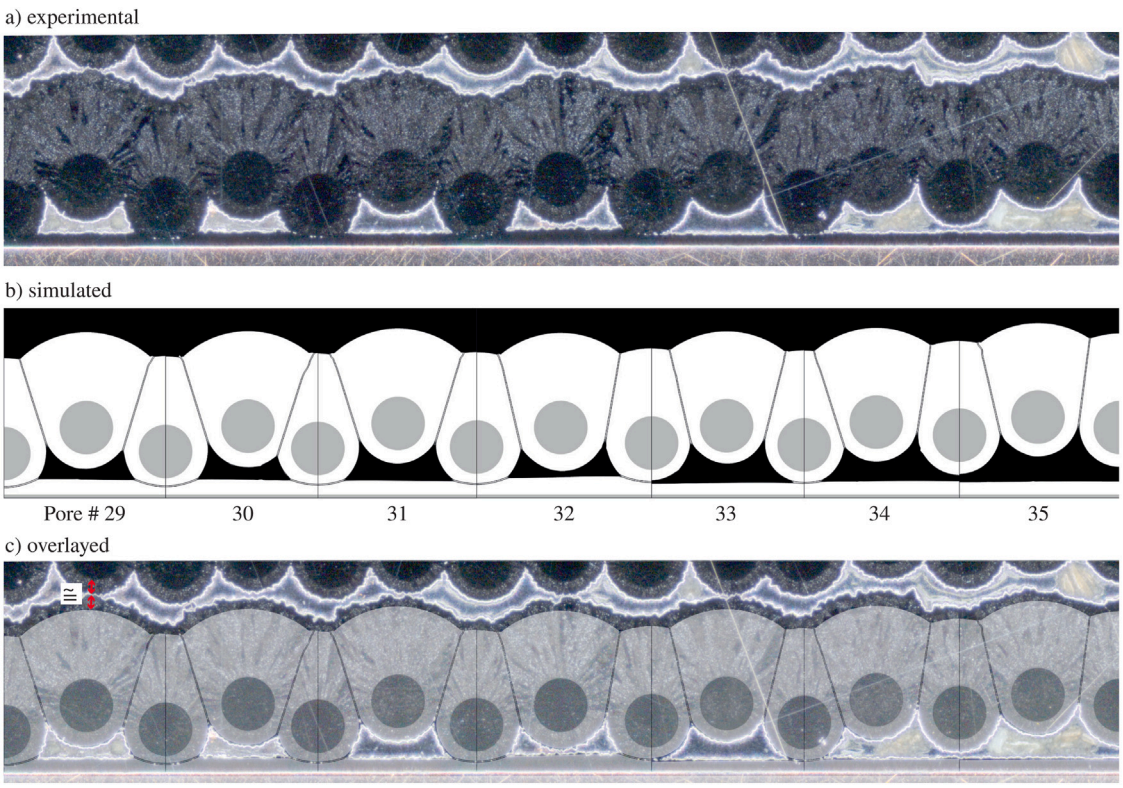

Fig. 19. Pore structure result comparison example for pore #29–35. (a) section of the dark field microscopic image of the experimental result, (b) concatenation of the seven single pore simulation results (c) overlay.

Furthermore, in Fig. 16c–d can be seen that the major partial pressure (p) gradient, within the scale of a single pore, is radial for H_2 and vertical for WF_6. The reason for this behavior is the difference in their molecule size and mass, and thus in their diffusion coefficients. The fast diffusing H_2 molecules can flatten the gradient towards the heating plate caused by the consumption of the precursors. However, for the slow WF_6 molecules, the supply via diffusion cannot compensate the consumption completely (a higher heating temperature increases the gradients even further). If the CVD process is driven in H_2 over-stoichiometry (H_2:WF_6 > 3:1), as it was done in the present work, WF_6 is the deposition rate limiting precursor [32]. This fact added to the fact that for p_{WF_6} the major gradient is vertical is also the reason for that in the Single Pore Model the species fluxes at the geometric side boundaries could be set to zero.

In the following Fig. 17, p_i line plots along the red lines in the zoomed sections in Fig. 16 are shown. The red lines are at the same height as the upper boundary of the Single Pore Model and thus these values of the Reactor Model were taken as input for the Single Pore Model. Additionally p_{HF} is plotted, which increases radially according to Eq. (1).

For comparison, constant calculated estimations for p_i were added, which base solely on the inlet gas flow ratios and the total pressure (dashed lines). The simulated p_{H_2} starts lower than in the simple estimation, since HF is already present in the center. However, interestingly, the simulated p_{WF_6} near the center is actually higher than in the estimation. The reason can be seen by comparing Fig. 16(c) to (d): Within the gas shower the light H_2 molecules diffuse outwards much faster than the heavy and WF_6 molecules, which increases p_{WF_6} in the center.

4.3. Single Pore Model

In Fig. 18 an example for the growing W coating (white) on multiple fibers (gray) is shown with a color map for p_{WF_6} in the gaseous domain. For t = 0 to 8 min the pore entrance becomes narrower, p_{WF_6} decreases within the pore and the diffusive flux increases due to larger concentration gradient. At t = 10 min the right entrance is sealed (or quasi-sealed, since an artificial gap remains). Due to the implementation of Knudsen diffusion, the diffusive flux within the artificial gap is reduced so strongly that the diffusive flux in the upper right part of the pore switched its direction, which would be also reasonable without an artificial gap, as in reality. At t = 11 min the pore is almost completely sealed. The diffusive flux through the remaining left entrance is maximal and p_{WF_6} within the pore is near zero, since WF_6 is still consumed. Between t = 11 to 13 min the pore is completely (quasi-)sealed. From now on R_W as well as the consumption of WF_6 are set to zero within the pore by Eq. (7). Due to the diffusion through the remaining artificial gaps, the pore is filled with WF_6 again, which would not happen in reality. In reality p_{WF_6} would stay zero (dark blue) within the pore for $t \geq 13$ min. This could not be achieved in the simulation, since setting the diffusion coefficient to zero within the artificial gaps resulted in infinitely high gas concentration gradients so that the simulation could not converge and thus failed. However, the resulting pore structure and the microscaled relative density (ρ_{rel}) should still be correct, since they do not change anymore once the pore got quasi sealed. Only the coating on top of the fibers continues to grow until the deposition process is stopped at t = 45 min, as in reality.

Similar as described above, all 45 pore shapes were simulated and their corresponding ρ_{rel} calculated. More detailed results are shown in the following section while being directly compared to the experimental results.

4.4. Simulated vs. experimental results

In Fig. 19 an example for the graphical comparison between the experimental and simulated W_f/W pore structure is shown (Pores #29–35). As it can be seen in the overlay (c), the match is very good. The pore structure looks identical. The experimental coating thickness on

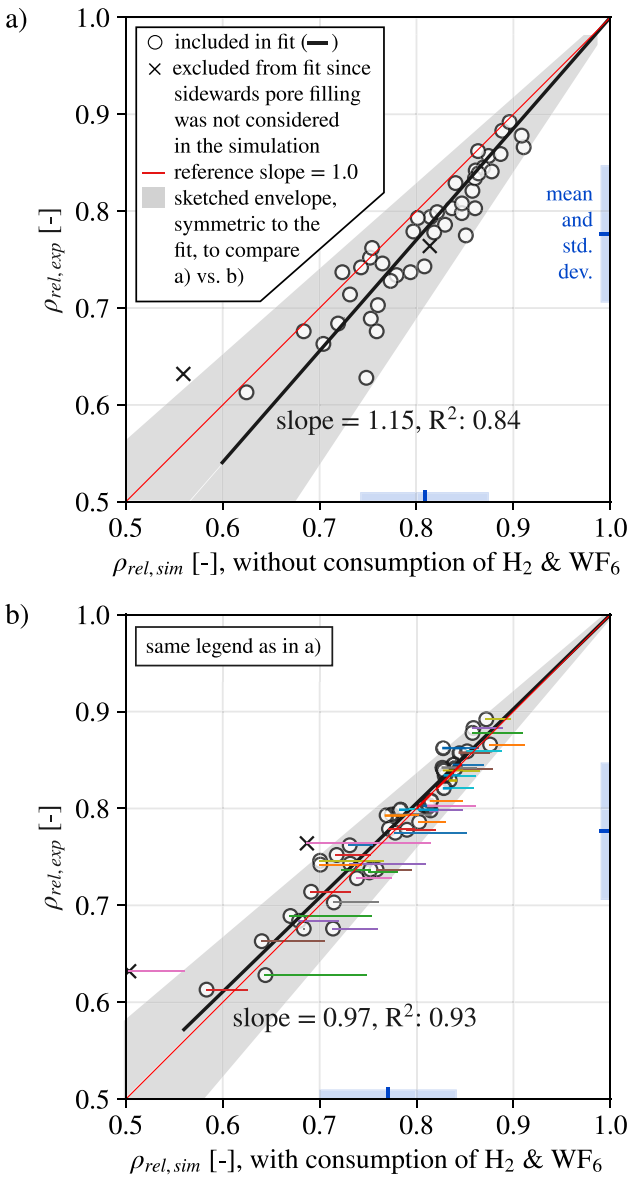

Fig. 20. Experimental relative density ($\rho_{rel,exp}$) vs. simulated relative density ($\rho_{rel,sim}$). (a) Simulated *without* precursor consumption and thus with a constant W deposition rate (R_W). (b) Simulated *with* precursor consumption and thus with a spatially and transiently changing R_W. The thin colored horizontal lines in (b) mark the shift of the $\rho_{rel,sim}$ data points from (a) to (b). (For interpretation of the references to color in this figure legend, the reader is referred to the web version of this article.)

top of the first layer of fibers is a bit higher. However, as mentioned in Section 2.1, the sample was produced with multiple fabric layers in the frame-work of an experimental fiber–fiber-distance parameter study [34]. After subtracting the coating thickness below the fibers of the second layer (red arrows in Fig. 19c), also the coating thickness on top of the first layer is well in agreement.

However, from just a visual overlay it is not possible to obtain a quantitative comparison of the pore sizes. It looks like that the CVD-W was deposited evenly along the surfaces within the pores (same coating thickness on the fiber and on the ground). If this was true, one could use a sole geometric approach with rectangles and circle segments to calculate ρ_{rel}, with no need to include the complicated precursor consumption and diffusion mechanisms into the model. To demonstrate that such an approach is indeed not sufficient, the experimental results are compared quantitatively at first to simulated results, in which R_W was set constant (by deactivating Comsol's transport of concentrated species interface so that the species concentrations remained at their initial values over the entire geometry). The result of this simplified comparison is shown in Fig. 20a. For this plot, the experimental and simulated ρ_{rel} data points were calculated as described in 2.2. Each data point (exp.-sim. pair) belongs to a certain pore-# with a certain substrate geometry (= fiber coordinates). The meaning of "pore-#" can be understood from Fig. 19b.

For two pore-#, the W deposition within the pore continued in the experiment after the upper pore entrance was sealed already. The reason was that the pore entrance of an adjacent pore-# was at least 33% larger than for the evaluated one. In addition, the fibers were positioned high enough so that in the experiment the precursors could still diffuse in sidewards below the side fibers of the investigated pore, after the top entrance was sealed already. This was not possible in the simulation due to simulating only one pore with a "no flux" condition at the side boundaries (Fig. 11a). Therefore, the two corresponding data points marked as (×) were excluded from the linear regression (black line) and all further statistics summarized in Table 4.

For a perfect match between simulated and experimental results, the data points would line up along the red 45°-line and the slope of the black regression line would be 1.0. In contrast, the regression line in Fig. 20a (pinned to the coordinates x–y = 1–1), has a slope of 1.15 with a coefficient of determination (R^2) of 0.84. The mismatch can be assumed to be caused mainly by the simulated $\rho_{rel,sim}$ being too large (too far right). The reason is that the precursor consumption was neglected in these simulations resulting in that most of the pores were filled much better in the simulation than in reality. Furthermore, it can be seen that this overestimation increases with decreasing ρ_{rel} (going from top right to bottom left). For lower ρ_{rel}, and thus larger pores, also the reaction surface area within the pore becomes larger. The larger the reaction surface, the more pronounced becomes the neglect of the precursor consumption and thus the overestimation of the pore filling.

By *including* the WF_6 and H_2 consumption (and HF formation), the fitting slope in improves from 1.15 to 0.97 as shown in Fig. 20b. By applying only the measuring uncertainties for the simulation input, which are summarized in Table 4, the fitting slope varies by ± 0.03. Thus, the slope of 0.97 is already within the range of the simulation input measuring uncertainties. Additionally, the scattering of the data points is reduced significantly by including the precursor consumption, which improves R^2 from 0.84 to 0.93. The reason is that the simulated data points are shifted by varying distances towards lower x-values (visualized as differently colored thin lines in Fig. 20b). This can be explained by the variations in the fiber positions and pore entrance sizes, which determine how strongly the precursor consumption affects the pore filling with CVD-W. In addition, as it can be seen from Table 4, by including consumption the sim.-to-exp. difference regarding the mean ρ_{rel} improves from 0.031 to 0.006, whereby only the latter is within the range of measuring uncertainties.

In an additional side-study the effect of the Knudsen diffusion on the simulation results has been investigated. The result can be also seen in Table 4. Including only the consumption, but not yet Knudsen diffusion reduced, the mean ρ_{rel} by 0.027 (first to second row in Table 4). Including additionally Knudsen diffusion, reduced ρ_{rel} by further 0.01 (second to third row). The reason is that by including Knudsen diffusion the precursor supply into the pore is reduced, which increases the R_W gradients towards the bottom end of each pore and thus increases the final pore sizes.

On the one hand, without Knudsen diffusion the fitting slope results in 1.02 and the difference to the experimental results in the mean ρ_{rel} is only 0.004, which matches both slightly better to the experimental results. On the other hand, the standard deviation of ρ_{rel} and R^2 matches slightly better with Knudsen diffusion. Since the simulations without and with Knudsen diffusion are both within the range of the measuring uncertainties, only one final thought: If in reality the pores were filled on average slightly more than in the simulation, the explanation could

Table 4
Differently simulated results vs. the experimental results; mean relative densities (ρ_{rel}), uncertainties, and standard deviations based on 43 data points as plotted as ∘-symbols in Fig. 20. The simulated uncertainties come from the simulation input. In detail, mainly from the fiber position uncertainties (±0.0049), and from the temperature and top boundary partial pressure uncertainties (±0.0022). The experimental uncertainties come from the pore size measurement.

	Precursor consumption	Knudsen diffusion	Dimensions	ρ_{rel} [%]			Linear regression exp. vs. sim.		Plotted in Fig. 20
				Mean	uncert.	std. dev.	Slope	R^2	
Simulated	No	No	2D	80.8	± ~0.5	±6.6	1.148	0.840	a
	Yes	No		78.1	± ~0.7	±6.7	1.020	0.929	–
	Yes	Yes		77.1	±0.71	±7.1	0.973	0.934	b
Experimental	Yes	Probably	3D	77.7	±1.1	±7.1	–		a + b

Table 5
Comsol mesh settings to meet the challenges of the transient Single pore infiltration model.

	In general	At W surface	At first contact
max element size	20 µm	10 µm	
min element size	0.8 µm		
max element growth rate	1.2	1.1	
Curvature factor	0.3	0.12	
Resolution of narrow regions	1		3

be, that in reality the precursors could diffuse along the not simulated third dimension. One can imagine that a 3D pore network has a better and longer averaged precursor supply if it is connected to a large pore entrance. Therefore, the simplification of no-Knudsen diffusion (easier pore infiltration) may have outweighed the 2D simplification (harder pore infiltration).

5. Conclusion and outlook

A model has been developed with Comsol Multiphysics to simulate the chemical vapor deposition/infiltration of closely adjacent W fibers by solid W. Furthermore, several workarounds for a pseudo surface-to-surface contact were successfully implemented in Comsol to simulate how growing CVD-W coatings can seal off gas domains.

The model results were compared to a metallographic cross section of a tungsten fiber reinforced tungsten (W_f/W) composite specimen containing 91 fibers. The model is capable of correctly describing the W deposition rate as well as the resulting W_f/W pore structure and microscaled relative densities within the measuring uncertainties (≃ ±1%). Key factors were the precursor transport and its consumption, which determine the partial pressure distribution macroscopically inside of the reactor as well as microscopically inside of the pores. At a given temperature, these partial pressure distributions determine the W deposition rates and thus the coating shapes inside of the pores.

The model presented and validated here was applied in a CVD process parameter study for the W_fW synthesis, in which relative density, coating uniformity, WF_6 demand, and process time were optimized [47,48]. These results are likely to be transferable and thus useful for other CVD applications as well.

CRediT authorship contribution statement

L. Raumann: Methodology, Investigation, Validation, Visualization, Writing – original draft, Countless scientific discussions, Ongoing feedback and suggestions, Writing – review & editing. **J.W. Coenen:** Conceptualization, Supervision, Countless scientific discussions, Ongoing feedback and suggestions, Writing – review & editing. **J. Riesch:** Conceptualization, Supervision, Countless scientific discussions, Ongoing feedback and suggestions, Writing – review & editing. **Y. Mao:** Conceptualization, Countless scientific discussions, Ongoing feedback and suggestions, Writing – review & editing. **D. Schwalenberg:** Investigation, Countless scientific discussions, Ongoing feedback and suggestions, Writing – review & editing. **T. Wegener:** Software, Countless scientific discussions, Ongoing feedback and suggestions, Writing – review & editing. **H. Gietl:** Methodology, Countless scientific discussions, Ongoing feedback and suggestions, Writing – review & editing. **T. Höschen:** Conceptualization, Countless scientific discussions, Ongoing feedback and suggestions, Writing – review & editing. **Ch. Linsmeier:** Funding acquisition, Project administration, Countless scientific discussions, Ongoing feedback and suggestions, Writing – review & editing. **O. Guillon:** Supervision, Countless scientific discussions, Ongoing feedback and suggestions, Writing – review & editing.

Declaration of competing interest

The authors declare that they have no known competing financial interests or personal relationships that could have appeared to influence the work reported in this paper.

Acknowledgments

Many thanks to Beatrix Goths for metallographic assistance, to our staff members Rudi Caspers, Dirk Nicolai, Tim Ruttgers, Robert Habrichs, and Albert Hiller for experimental assistance, and to the Python community.

This work has been carried out within the framework of the EUROfusion Consortium and has received funding from the Euratom research and training programme 2014–2018 and 2019–2020 under grant agreement No 633053. The views and opinions expressed herein do not necessarily reflect those of the European Commission.

Appendix A

A.1. Mesh and solver configurations in Comsol for the Single Pore Model

The time-dependent solver was set to ensure element distortions < 1.1 and as option for a consistent initialization "Backward Euler" was chosen. Further, the maximum simulated time step size was limited to 5 s. The settings for the automated initial meshing and remeshing are listed in Table 5. The general and coarser settings are applied on the complete model geometry. To account for near surface steep gradients in p_i and L_{char}, the elements along the W surface were limited in their maximum size and growth. Further, around the pseudocontact and in the area of the moving entrance of the artificial gap, quantities such as the wall distances, the diffusion coefficient, and the wall velocity (equal to R_W) change spatially rapidly. Therefore, despite of the smoothed deceleration of R_W, a very high mesh resolution is still necessary to avoid the simulation crashing due to discontinuities. To further increase the mesh resolution only where needed, the curvature factor at the W surface is decreased significantly. A lower curvature factor causes more elements to be used to approximate the true shape of a curve. As the curvature of the W surface is particularly high at the entrance of the artificial gap, a high mesh resolution is created automatically only where needed. Finally, the resolution of narrow regions was increased from 1 to 3 where the first contact takes place.

The resulting mesh deformation and automated remeshing is shown in Fig. 21. The subplots for six time-steps show close-ups of the pseudocontact between two CVD-W surfaces growing on adjacent fibers.

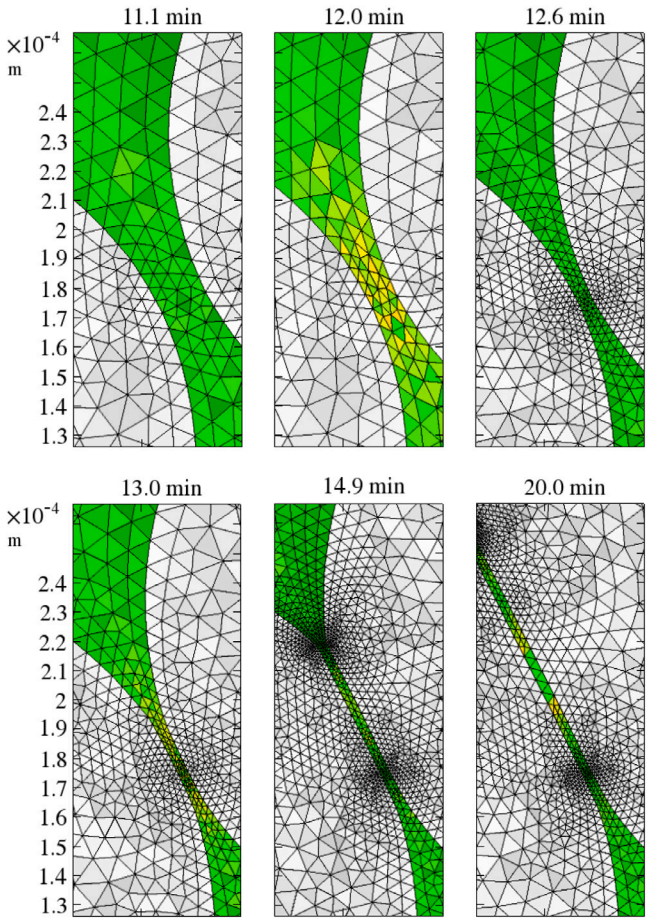

Fig. 21. Mesh evolution during a CVD-W pseudocontact. The filling color of the elements illustrates the element skewness, which is a measure for the element quality. For a perfect quality all 3 inner angles equal 60°, shown in green in the gas and in white in the solid domain. Elements with a bad quality would be red in the gas and black in the solid domain. As it can be seen, the element quality remains good. (For interpretation of the references to color in this figure legend, the reader is referred to the web version of this article.)

From 11.1 to 12.0 min, the mesh movement can still be covered by mesh deformation, since it only slightly reduces the element quality between the fibers. At 12.6 min, the element deformation would be too high. Therefore, a remeshing is done resulting in a finer mesh without mesh deformation around the contact point due to the adjustment of the resolution of narrow regions. Between 13.0 and 14.9 min the pore is sealed, the lower part no longer moves. The upper part continues to grow, while the fine mesh area moves upwards. The meshing settings (Table 5) allow also for a recovery to a coarser mesh, where a fine mesh is no longer required. For example at 20.0 min the artificial gap width is resolved by only one element, if it is far enough away from sharp surface radii, which saves computational time.

Appendix B. Supplementary data

Supplementary material related to this article can be found online at https://doi.org/10.1016/j.nme.2021.101048.

References

[1] F. Romanelli, Fusion Electricity a roadmap to the realisation of fusion energy, in: European Fusion Development Agreement, EFDA, ISBN: 978-3-00-040720-8, 2012.

[2] G. Federici, G. Giruzzi, C. Lowry, R. Kemp, D. Ward, R. Wenninger, H. Zohm, EU DEMO design and R & D studies, in: Fusion Engineering (SOFT), 2013 IEEE 25th Symposium on Fusion Technology, 2013, pp. 1–8.

[3] H. Zohm, Assessment of DEMO challenges in technology and physics, Fusion Eng. Des. 88 (6–8) (2013) 428–433.

[4] R. Wenninger, M. Bernert, T. Eich, E. Fable, G. Federici, A. Kallenbach, A. Loarte, C. Lowry, D. McDonald, R. Neu, T. Pütterich, P. Schneider, B. Sieglin, G. Strohmayer, F. Reimold, M. Wischmeier, DEMO divertor limitations during and in between ELMs, Nucl. Fusion 54 (11) (2014) 114003.

[5] N. Baluc, Materials for fusion power reactors, Plasma Phys. Control. Fusion 48 (12B) (2006) B165–B177.

[6] Ch. Linsmeier, M. Rieth, J. Aktaa, T. Chikada, A. Hoffmann, J. Hoffmann, A. Houben, H. Kurishita, X. Jin, M. Li, A. Litnovsky, S. Matsuo, A. von Müller, V. Nikolic, T. Palacios, R. Pippan, D. Qu, J. Reiser, J. Riesch, T. Shikama, R. Stieglitz, T. Weber, S. Wurster, J.-H. You, Z. Zhou, Development of advanced high heat flux and plasma-facing materials, Nucl. Fusion 57 (9) (2017) 092007.

[7] X. Yang, A. Hassanein, Atomic scale calculations of tungsten surface binding energy and beryllium-induced tungsten sputtering, Appl. Surf. Sci. 293 (2014) 187–190.

[8] D.P. Jackson, Binding energies in cubic metal surfaces, Radiat. Eff. 18 (3–4) (1973) 185–189.

[9] E. Lassner, W.-D. Schubert, Tungsten - Properties, Chemistry, Technology of the Element, Alloys, and Chemical Compound, Springer, 1999.

[10] J. Reiser, M. Rieth, B. Dafferner, A. Hoffmann, Charpy impact properties of pure tungsten plate material in as-received and recrystallized condition, J. Nucl. Mater. 442 (2013) 204–207.

[11] H. Bolt, V. Barabash, G. Federici, J. Linke, A. Loarte, J. Roth, K. Sato, Plasma facing and high heat flux materials – needs for ITER and beyond, J. Nucl. Mater. 307–311 (1) (2002) 43–52.

[12] J.W. Coenen, S. Antusch, M. Aumann, W. Biel, J. Du, J. Engels, S. Heuer, A. Houben, T. Höschen, B. Jasper, et al., Materials for DEMO and reactor applications – boundary conditions and new concepts, Phys. Scr. (T167) (2016).

[13] G. Pintsuk, I. Bobin-Vastra, S. Constans, P. Gavila, M. Rödig, B. Riccardi, Qualification and post-mortem characterization of tungsten mock-ups exposed to cyclic high heat flux loading, Fusion Eng. Des. 88 (9–10) (2013) 1858–1861, proceedings of the 27th Symposium On Fusion Technology (SOFT-27); Liège, Belgium, September (2012) 24-28.

[14] J.W. Coenen, Fusion Materials Development at Forschungszentrum Jülich, Adv. Energy Mater. 22 (6) (2020) 1901376.

[15] J.W. Coenen, Y. Mao, S. Sistla, J. Riesch, T. Höschen, C. Broeckmann, R. Neu, Ch. Linsmeier, Improved pseudo-ductile behavior of powder metallurgical tungsten short fiber-reinforced tungsten (W_f/W), Nucl. Mater. Energy 15 (2018) 214–219.

[16] R. Neu, J. Riesch, J.W. Coenen, J. Brinkmann, A. Calvo, S. Elgeti, C. Garcia-Rosales, H. Greuner, T. Höschen, G. Holzner, F. Klein, F. Koch, Ch. Linsmeier, A. Litnovsky, T. Wegener, S. Wurster, J.-H. You, Advanced tungsten materials for plasma-facing components of DEMO and fusion power plants, Fusion Eng. Des. 109-111: Part A (2016) 1046–1052.

[17] R. Neu, J. Riesch, A. Müller, M. Balden, J.W. Coenen, H. Gietl, T. Höschen, M. Li, S. Wurster, J.-H. You, Tungsten fibre-reinforced composites for advanced plasma facing components, Nucl. Mater. Energy 12 (2016) 1308–1313.

[18] J. Riesch, M. Aumann, J.W. Coenen, H. Gietl, G. Holzner, T. Höschen, P. Huber, M. Li, Ch. Linsmeier, R. Neu, Chemically deposited tungsten fibre-reinforced tungsten - The way to a mock-up for divertor applications, Nuclear Mater. Energy 9 (75).

[19] J. Riesch, Y. Han, J. Almanstötter, J.W. Coenen, T. Höschen, B. Jasper, P. Zhao, Ch. Linsmeier, R. Neu, Development of tungsten fibre-reinforced tungsten composites towards their use in DEMO - potassium doped tungsten wire, Phys. Scr. 2016 (T167) (2016) 014006.

[20] H. Gietl, S. Olbrich, J. Riesch, G. Holzner, T. Höschen, J.W. Coenen, R. Neu, Estimation of the fracture toughness of tungsten fibre-reinforced tungsten composites, Eng. Fract. Mech. (2020) 107011.

[21] K.K. Chawla, Ceramic Matrix Composites, second ed., Springer US, New York, 2003.

[22] J. Riesch, Entwicklung Und Charakterisierung Eines Wolframfaserverstärkten Wolfram-Verbundwerkstoffs (Ph.D. thesis), Technische Universität München, 2012.

[23] J. Riesch, J.-Y. Buffiere, T. Höschen, M. di Michiel, M. Scheel, Ch. Linsmeier, J.-H. You, In situ synchrotron tomography estimation of toughening effect by semi-ductile fibre reinforcement in a tungsten-fibre-reinforced tungsten composite system, Acta Mater. 61 (19) (2013) 7060–7071.

[24] Y. Mao, J.W. Coenen, J. Riesch, S. Sistla, J. Almanstötter, B. Jasper, A. Terra, T. Höschen, H. Gietl, M. Bram, et al., Development and characterization of powder metallurgically produced discontinuous tungsten fiber reinforced tungsten composites, Phys. Scr. 2017 (T170) (2017) 014005.

[25] Y. Mao, J.W. Coenen, J. Riesch, S. Sistla, J. Almanstötter, B. Jasper, A. Terra, T. Höschen, H. Gietl, Ch. Linsmeier, C. Broeckmann, Influence of the interface strength on the mechanical properties of discontinuous tungsten fiber-reinforced tungsten composites produced by field assisted sintering technology, Composites A 107 (2018) 342–353.

[26] J.W. Coenen, Y. Mao, S. Sistla, A. Müller, G. Pintsuk, M. Wirtz, J. Riesch, T. Höschen, A. Terra, J.-H. You, H. Greuner, A. Kreter, C. Broeckmann, R. Neu, Ch. Linsmeier, Materials development for new high heat-flux component mock-ups for DEMO, Fusion Eng. Des. 146 (2019) 1431–1436.
[27] H. Gietl, A. v Müller, J.W. Coenen, M. Decius, D. Ewert, T. Höschen, P. Huber, M. Milwich, J. Riesch, R. Neu, Textile preforms for tungsten fibre-reinforced composites, J. Compos. Mater. 52 (28) (2018) 3875–3884.
[28] H. Gietl, J. Riesch, J.W. Coenen, T. Höschen, R. Neu, Production of tungsten-fibre reinforced tungsten composites by a novel continuous chemical vapour deposition process, Fusion Eng. Des. 146 (2019) 1426–1430.
[29] A.F. Zinn, The Chemistry of Metal CVD, VCH Verlagsgesellschaft, Weinheim, 2007, pp. 105–174, Chapt. Chemical vapor deposition of tungsten.
[30] H. Gietl, J. Riesch, J.W. Coenen, T. Höschen, Ch. Linsmeier, R. Neu, Tensile deformation behavior of tungsten fibre-reinforced tungsten composite specimens in as-fabricated state, Fusion Eng. Des. 124 (2017) 396–400.
[31] COMSOL INC. URL: https://www.comsol.com/.
[32] L. Raumann, J.W. Coenen, J. Riesch, Y. Mao, H. Gietl, T. Höschen, Ch. Linsmeier, O. Guillon, Modeling and validation of chemical vapor deposition of tungsten for tungsten fiber reinforced tungsten composites, Surf. Coat. Technol. 381 (2020) 124745.
[33] H. Gietl, Weiterentwicklung Von Wolframfaserverstfärktem Wolframverbundwerkstoff Für Den Einsatz in Der Fusion (Ph.D. thesis), Technische Universität München, 2018.
[34] H. Gietl, A. Müller, J. Riesch, J.W. Coenen, T. Höschen, P. Huber, M. Decius, D. Ewert, M. Milwich, R. Neu, Textile preforms for tungsten fibre-reinforced composites, J. Compos. Mater. 52 (28) (2018) 3875–3884.
[35] Python library Skimage. URL: https://scikit-image.org/docs/dev/api/skimage.html.
[36] Raumann, Github repository for the model and script files of the present work, 2020, URL: https://github.com/Leo-Raumann/Dissertation-Files.git.
[37] E.J. McInerney, E. Srinivasan, D.C. Smith, G. Ramanath, Kinetic rate expression for tungsten chemical vapor deposition in different WF_6 flow regimes from step coverage measurements, Z. Met.kd. 91 (2000) 573–580.
[38] I. Barin (Ed.), Thermochemical Data of Pure Substances, VCH Verlagsgesellschaft, Weinheim, 1995.
[39] J.O. Hirschfelder, C.F. Curtiss, R.B. Bird, The Molecular Theory of Gases and Liquids, John Wiley & Sons, Inc, New York, 1964.
[40] C.R. Kleijn, C. Werner, Modeling of Chemical Vapor Deposition of Tungsten Films, Birkhäuser, Basel, 1993.
[41] K. Kuijlaars, C. Kleijn, H. Van Den Akker, Multi-component diffusion phenomena in multiple-wafer chemical vapour deposition reactors, Chem. Eng. J. Biochem. Eng. J. 57 (2) (1995) 127–136.
[42] T. Oosterlaken, G. Leusink, G. Janssen, S. Radelaar, The hydrogen reduction of WF_6: A kinetic study based on in situ partial pressure measurements, J. Electrochem. Soc. 143 (5) (1996) 1668–1675.
[43] C. Kleijn, C. Hoogendoorn, A. Hasper, J. Holleman, J. Middelhoek, Transport Phenomena in Tungsten LPCVD in a single-wafer reactor, J. Electrochem. Soc. 138 (2) (1991) 509–517.
[44] M. Knudsen, The Kinetic Theory of Gases, John Wiley & Sons, Inc., New York, 1950.
[45] A. Hasper, Modeling and optimization of the step coverage of Tungsten LPCVD in trenches and contact holes, J. Electrochem. Soc. 138 (6) (1991) 1728.
[46] D.F. Fairbanks, C.R. Wilke, Diffusion coefficients in multicomponent gas mixtures, Ind. Eng. Chem. 42 (3) (1950) 471–475.
[47] L. Raumann, Modeling and validation of chemical vapor deposition for tungsten fiber reinforced tungsten, in: Schriften des Forschungszentrums Juelich – Energy and Environment, vol. 515, Forschungszentrum Jülich GmbH, 2020.
[48] L. Raumann, J.W. Coenen, J. Riesch, Y. Mao, H. Gietl, Ch. Linsmeier, O. Guillon, Improving the W coating uniformity by a COMSOL model-based CVD parameter study for denser Wf/W composites, Metals 11 (7) (2021) 1089.